Front. Chem. Sci. Eng. 2021, 15(6): 1500–1513
https://doi.org/10.1007/s11705-021-2086-2

RESEARCH ARTICLE

Carbon-doped surface unsaturated sulfur enriched CoS_2@rGO aerogel pseudocapacitive anode and biomass-derived porous carbon cathode for advanced lithium-ion capacitors

Yunpeng Shang[1], Xiaohong Sun (✉)[1], Zhe Chen[1], Kunzhou Xiong[1], Yunmei Zhou[1], Shu Cai[1], Chunming Zheng (✉)[2]

1 School of Materials Science and Engineering, Key Laboratory of Advanced Ceramics and Machining Technology of Ministry of Education, Tianjin University, Tianjin 300072, China
2 School of Chemistry and Chemical Engineering, State Key Laboratory of Hollow Fiber Membrane Materials and Membrane Processes, Tiangong University, Tianjin 300387, China

Abstract As a hybrid energy storage device of lithium-ion batteries and supercapacitors, lithium-ion capacitors have the potential to meet the demanding needs of energy storage equipment with both high power and energy density. In this work, to solve the obstacle to the application of lithium-ion capacitors, that is, the balancing problem of the electrodes kinetic and capacity, two electrodes are designed and adequately matched. For the anode, we introduced *in situ* carbon-doped and surface-enriched unsaturated sulfur into the graphene conductive network to prepare transition metal sulfides, which enhances the performance with a faster lithium-ion diffusion and dominant pseudocapacitive energy storage. Therefore, the lithium-ion capacitors anode material delivers a remarkable capacity of 810 $mAh \cdot g^{-1}$ after 500 cycles at 1 $A \cdot g^{-1}$. On the other hand, the biomass-derived porous carbon as the cathode also displays a superior capacity of 114.2 $mAh \cdot g^{-1}$ at 0.1 $A \cdot g^{-1}$. Benefitting from the appropriate balance of kinetic and capacity between two electrodes, the lithium-ion capacitors exhibits superior electrochemical performance. The assembled lithium-ion capacitors demonstrate a high energy density of 132.9 $Wh \cdot kg^{-1}$ at the power density of 265 $W \cdot kg^{-1}$, and 50.0 $Wh \cdot kg^{-1}$ even at 26.5 $kW \cdot kg^{-1}$. After 10000 cycles at 1 $A \cdot g^{-1}$, lithium-ion capacitors still demonstrate the high energy density retention of 81.5%.

Keywords *in-situ* carbon-doped, surface unsaturated sulfur enriched, pseudocapacitive energy storage, biomass-derived carbon, lithium-ion capacitors

Received March 27, 2021; accepted June 16, 2021

E-mails: sunxh@tju.edu.cn (Sun X), zhengchunming@tiangong.edu.cn (Zheng C)

1 Introduction

The continuous advances of industry and technology have made aerospace, portable equipment, large-scale energy storage, especially hybrid electric vehicle, and many other fields more urgent for energy storage technology with high energy/power density [1]. As a new type of energy storage device, lithium-ion capacitors (LICs) can integrate the advantages of supercapacitors (SCs) and lithium-ion batteries (LIBs) to partly avoid suffering from the low power density as well as poor cycle performance of LIB and low energy density of SC [2]. Generally, LIC is composed of a battery-type anode and capacitor-type cathode with relatively high energy/power density between SC and LIB [3]. Although the LIC research has gained exciting achievements recently, the high energy density of LIC can only demonstrate at low power densities in most cases. Such a defect is caused by the slow lithium-ion diffusion and electrochemical reaction kinetics of the anode, which significantly reduces the commercial application values of LIC. To solve the intrinsic imbalance of kinetic and capacity between two electrodes of LIC, developing anode materials with faster lithium-ion diffusion and charge transfer along with a larger capacity cathode is the focus of current LIC research [3].

For a long time, transition metal sulfides (TMSs) have been widely studied for energy storage due to their excellent electrical conductivity and structural stability [4,5]. Although TMS has tremendous potential for

high-performance LIC anodes as well, there are few reports about it [4–6]. Among various TMSs, CoS_2 is an attractive candidate for LIC anode because of its high-profile electrochemical properties as the anode of lithium/sodium-ion batteries [7]. It is more common that the reduced graphene oxide (rGO) hydrogel randomly self-assembled during the hydrothermal process has been used as an effective composite carrier to improve the performance of the TMS anode [2]. This highly conductive three-dimensional framework can undoubtedly enhance the kinetics of the electrode material by accelerating electron transfer and shortening the ion diffusion path. It can also accommodate the volumetric variation of the electrode material during charge/discharge to improve cycle stability [8]. Furthermore, *in situ* carbon doping as the second conductive network in the bulk phase of CoS_2 can composite CoS_2 with the three-dimensional rGO aerogel to maximize the reaction kinetics [9]. On the other hand, the newly developed strategy of increasing the contribution of the surface pseudocapacitive energy storage is also particularly significant in accelerating the kinetic [2]. From the research results of Augustyn et al., the capacity of the anode is mainly composed of surface pseudocapacitive energy storage and bulk diffusion-controlled energy storage [10]. The pseudocapacitive energy storage is undoubtedly faster in kinetic than the other and causes less damage to the electrode. Therefore, adjusting the anode energy storage characteristic to lean toward capacitors can improve the slow and unbalanced kinetic. Based on the above analysis, in this work, the carbon-doped surface unsaturated sulfur-rich CoS_2@rGO aerogel anode has been successfully prepared. *In situ* doped carbon and graphene hydrogel build a dual high-efficiency three-dimensional conductive network to accelerate the kinetic of CoS_2. Surface-rich unsaturated sulfur can be used as lithium storage active sites and change the activity of surrounding reaction sites by affecting the electronic structure of them, thus increasing the contribution of surface pseudocapacitive energy storage and further accelerating the kinetic [11]. After analysis and verification by galvanostatic intermittent titration technique and electrochemical impedance spectroscopy, the unique structure of the prepared CoS_2 indeed improved the diffusion coefficient and charge transfer rate of lithium ions. L-cysteine plays a decisive role in the formation of such a characteristic structure, and similar results have been reported several times before as well [9,11,12].

For LIC cathodes, considering the cost and long-term cycle stability, activated carbon materials have been most commonly used. Among them, activated carbon derived from tree leaves as raw materials are not only low in cost but also beneficial to environmental protection [13]. Crabapple trees are widely planted in China and are mainly used for city afforestation and ornamental purposes with low economic value. The number of fallen leaves is very considerable, and its disposal requires a lot of overhead every year. So, using it as raw material for activated carbon seems to be a win-win choice. By exploring the full potential of Begonia leaves for activated carbon, a biomass-derived porous carbon suitable for LIC cathode has been successfully obtained in this work. The well-distributed mesopores greatly promote the rapid diffusion of ions, thereby improving the utilization of specific surface area and obtaining superior electrochemical performance. After being cycled for 5000 weeks at a high current density of 1 $A \cdot g^{-1}$, the specific capacity retention rate is still as high as 66.3%.

Unsurprisingly, thanks to the proper balance of kinetics and capacity between the two electrodes, the assembled LIC exhibits stable and excellent electrochemical performance and ultra-high energy/power density. The LIC demonstrates a high energy density of 132.9 $Wh \cdot kg^{-1}$ at a power density of 265 $W \cdot kg^{-1}$, and a high energy density of 50.0 $Wh \cdot kg^{-1}$ even at a power density of 26.5 $kW \cdot kg^{-1}$.

2 Experimental

2.1 Synthesis of carbon-doped surface unsaturated sulfur enriched CoS_2@rGO aerogel

Here, three samples were synthesized in a facile one-step hydrothermal method. Typically, 160 mg of graphene oxide (GO) powder was mixed in 80 mL of deionized water followed by sonication for 5 h, during which the temperature of GO dispersion was kept below 40 °C. After that, 0.2328 g $Co(NO_3)_2 \cdot 6H_2O$ and 0.3872 g L-cysteine were then added to the GO dispersion and stirred for 30 min to get fully pre-reactive, followed by a hydrothermal reaction process at 180 °C for 24 h. The cylindrical hydrogels obtained by the hydrothermal method were thoroughly cleaned with deionized water and then freeze-dried for 48 h. The carbon-doped surface unsaturated sulfur enriched CoS_2@rGO aerogel composite was denoted as CS-CoS_2@rGO. Carbon-doped surface unsaturated sulfur increased CoS_2 without compositing rGO aerogel (marked as CS-CoS_2) was also prepared for further characterization and analysis of the composition and structure of CS-CoS_2@rGO. Moreover, to compare and analyze the effect of the unique design on the electrochemical properties of CS-CoS_2@rGO, 0.2379 g $CoCl_2 \cdot 6H_2O$ and 0.248 g NaS_2O_3 with no carbon source was also used to prepare CoS_2@rGO aerogel composite (denoted as CoS_2@rGO) without doped carbon and unsaturated sulfur under the same conditions.

2.2 Synthesis of biomass-derived porous carbon

Three different kinds of samples were prepared by two synthetic routes to explore the full potential of crabapple leaves for activated carbon. The first involves washing, drying, grinding leaves into a fine powder and then

carbonizing at 600 °C for 2 h in an argon atmosphere. The obtained biochar and quadruple mass KOH were dispersed in deionized water and stirred for 12 h, followed by drying and grinding. The ground powder was activated under argon at 800 °C for 2 h, and then washed thoroughly with 1 mol·L^{-1} HCl and deionized water. After drying overnight in an oven at 80 °C, biomass-derived porous carbon was obtained. According to the different raw materials, the activated carbon derived from dead leaves was denoted as C-D, and the activated carbon derived from green leaves was marked as C-G. The second synthesis route is to disperse 1.5 g aforementioned dead leaves powder and 2.5 mL concentrated sulfuric acid into 50 mL of deionized water, followed by hydrothermal treatment at 180 °C for 48 h. After centrifugal collection, rinse with water, and dry, the obtained biochar was activated under the same conditions as the first preparation route. The finally prepared activated carbon prepared from the hydrothermal method was marked as C-H.

2.3 Materials characterization

Cathode and anode materials were characterized by scanning electron microscopy (SEM, Hitachi, S4800), energy dispersive spectrometer (EDS, Oxford Instruments, X-MAX20), nitrogen adsorption/desorption isotherms (Quantachrome, Nova 2200e), transmission electron microscopy (TEM, JEOL, JEM-2100F), X-ray diffraction (XRD, Bruker, D8 Advanced), thermogravimetric tests (TG, NETZSCH, STA499C), Raman spectra (RENISHAW, inVia reflex) and X-ray photoelectron spectrometry (XPS, Thermo Scientific, K-Alpha +).

2.4 Electrochemical measurements

First, the cathode and anode half-cells were assembled respectively to analyze their electrochemical characteristics. The electrode paste was composed of Super-P (10 wt-%), polyvinylidene difluoride (10 wt-%), active material (80 wt-%), and an appropriate amount of *N*-methyl-2-pyrrolidone. The Super-P is added here to ensure effective contact between the electrode material particles to give full play to the excellent conductivity of the material itself. The evenly mixed electrode slurry was coated on copper foil (for the anode) and aluminum foil (for cathode) and dried thoroughly in a vacuum oven at 120 °C. The working electrodes cut into discs, electrolyte (1 mol·L^{-1} $LiPF_6$ in a mixture of ethylene carbonate, diethyl carbonate, and ethyl methyl carbonate with equal volume), separator (Celgard 2400), and metal lithium counter electrode were assembled into 2032 button half cells in a glove box filled with argon. The LIC was built with the pre-lithiated CS-CoS_2@rGO anodes and C-D cathodes according to the operation mentioned above. The process of pre-lithiation was cycling the assembled CS-CoS_2@rGO half-cells at 0.1 A·g^{-1} for five cycles, then discharged to 0.5 V and kept it for two hours. The galvanostatic charge/discharge test (GCD, LAND CT2001A) of the cathode and anode half-cells were carried out at 1.5–4.3 V and 0.01–3 V, respectively. Cyclic voltammetry (CV) curves and electrochemical impedance spectroscopy (EIS) spectra (0.01–100 kHz) were obtained through the CHI660E electrochemical workstation. All the above tests were carried out at a constant room temperature of 25 °C.

3 Results and discussion

3.1 Characterization of anode materials

Graphene-free samples were prepared under the same conditions and labeled as CS-CoS_2 to analyze the structure and composition of carbon-doped surface unsaturated sulfur enriched CoS_2@rGO aerogel (CS-CoS_2@rGO). Besides, CoS_2@rGO with similar morphology as CS-CoS_2@rGO but without carbon doping or unsaturated sulfur was prepared to illustrate the changes in electrochemical performance. Figure 1 shows the morphological characteristics of these three materials. In the pre-reaction stage of CS-CoS_2 and CS-CoS_2@rGO, the $^-$NH and $^-$SH groups of L-cysteine coordinated with Co^{2+} ion to form complexes in the mixed solution [14]. These coordination groups were attracted by the oxygen-containing groups of graphene oxide and adsorbed on the graphene sheets [15]. With the temperature increasing during the hydrothermal process, H_2S generated from the decomposition of L-cysteine turned Co^{2+} into CoS_2, which could anchor to graphene sheets *in situ* [16]. The L-cysteine itself also formed a polymer network structure during the hydrothermal process [15]. If Co^{2+} was converted to CoS_2 in the case of uneven coordination with such a polymer network and effect of graphene spatial confinement, excess unsaturated sulfur might form on CoS_2 [17]. Graphene oxide was directly converted to rGO in the hydrothermal reaction of 180 °C and disorderedly stacked and linked to form a three-dimensional hydrogel structure in the action of π-π stacking [18].

From Fig. 1(a), CS-CoS_2 shows a regular octahedral structure, which is formed owing to the crystal preferential growth on the {111} facet with the lowest energy [19]. The morphology of CS-CoS_2@rGO presents small spherical clusters formed by several octahedral nanocrystals anchored on graphene sheets (Fig. 1(b)). The steric hindrance of graphene sheets is the dominant factor of a substantial reduction of the size of the crystals from CS-CoS_2 to CS-CoS_2@Rgo [16]. Therefore, the ion diffusion path of CS-CoS_2@rGO should be much shorter, which means faster ion diffusion and reaction kinetic [15,16]. The morphology of CoS_2@rGO is comparable to CS-CoS_2@rGO (Figs. 1(b) and 1(c)). As shown in Figs. 1(d) and 1(e), the calculated d-spacing of (111) plane and (220)

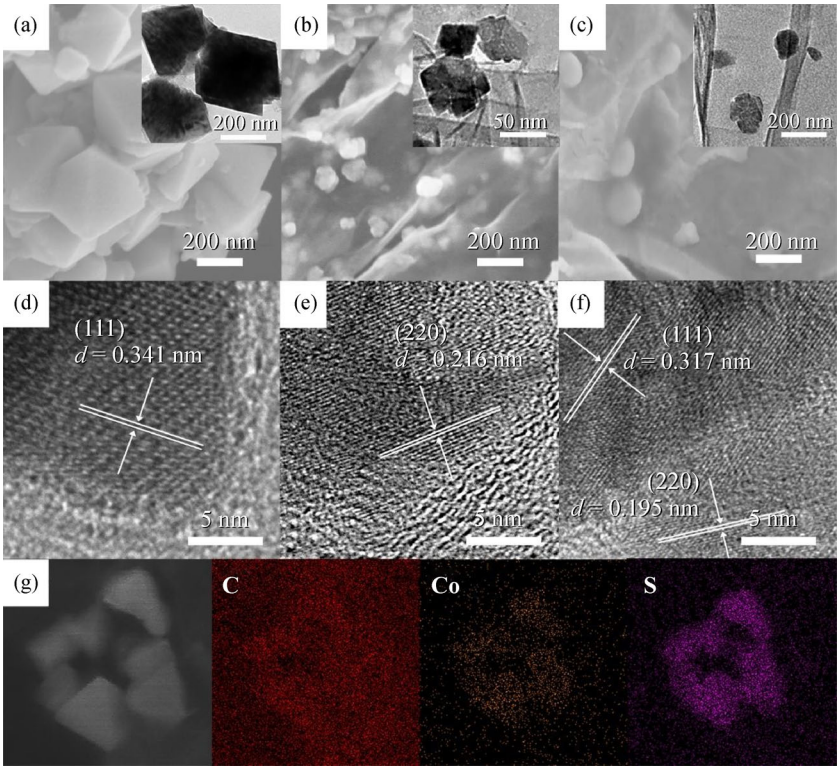

Fig. 1 SEM and TEM images of (a) CS-CoS_2, (b) CS-CoS_2@rGO, and (c) CoS_2@rGO; HRTEM images of (d) CS-CoS_2, (e) CS-CoS_2@rGO, and (f) CoS_2@rGO; (g) elemental mapping distribution of CS-CoS_2@rGO by EDS.

plane of CS-CoS_2 and CS-CoS_2@rGO are 0.341 and 0.216 nm, respectively. They are slightly larger than the standard d-spacing of cobalt sulfide (JCPDS NO.70-2865), where (111) plane should be 0.319 nm, and (220) plane should be 0.195 nm [10]. What is noteworthy is that the same two planes d-spacing of CoS_2@rGO did not increase in Fig. 1(f). The increase of interplanar spacing may stem from the interstitial incorporation of carbon during the hydrothermal process [13]. The carbon doping should be resulting from the pyrolysis of L-cysteine during hydrothermal and can be further proved by other subsequent characterizations [9]. The EDS maps of CS-CoS_2@rGO in Fig. 1(g) demonstrate that sulfur and cobalt elements are uniformly distributed. The distribution of the carbon element in the cobalt sulfide crystal range is more than that of the graphene matrix (Fig. 1(g)). Besides, the C element content analyzed by EDS in CS-CoS_2 is 8.58 at% (Table S1, cf. Electronic Supplementary Material, ESM). Based on the EDS analysis results, it can be inferred that the C element is doped into CS-CoS_2 as well as CS-CoS_2@rGO. The XRD, Raman spectrum, TG curve, and elemental composition information of these three materials are shown in Fig. 2. It can be seen from the XRD patterns in Fig. 2(a) that the diffraction peaks of CS-CoS_2, CS-CoS_2@rGO, and CoS_2@rGO are all in line with the standard card of CoS_2 crystals (JCPDS NO.70-2865). Remarkably, the (111) peak of CS-CoS_2 and (220) peak of CS-CoS_2@rGO both shows a slight shift of approximately 0.5° to the lower degrees, which also occurred to varying degrees on the other diffraction peaks of these two samples. The (111) interplanar spacing of CS-CoS_2 and (220) of CS-CoS_2@rGO calculated accurately by the Bragg Equation are 0.338 nm and 0.213 nm, respectively, which are correspond to the results of the TEM measurement. It should be the interstitial doping of carbon that leads to such diffraction peaks shift [20]. Also, there are no prominent diffraction peaks of graphite in the XRD patterns of CS-CoS_2 and CS-CoS_2@rGO, which may be due to the low content of doped carbon and the low crystallinity of rGO, respectively [21].

In Fig. 2(b), the Raman spectra of all show typical D-band (around 1350 cm^{-1}) and G-band (about 1580 cm^{-1}) peaks of carbon-based materials [22]. Among them, the ID/IG value (intensity ratio of above two bands) of CS-CoS_2@rGO is far higher than that of CoS_2@rGO, which can be inferred that the graphene sheets in CS-CoS_2@rGO are more disordered [22]. The difference in the degree of disorder of the graphene sheets in the two samples is mainly due to the use of different synthetic raw materials. The abundant defects can be used as active sites and have been proved to be beneficial to the improvement of electrochemical properties by many reports [11].

The TG test of these three samples was carried out immediately after being dried in a vacuum oven for 24 h to eliminate the influence of the material's adsorption of water on the test results. The experimental results are

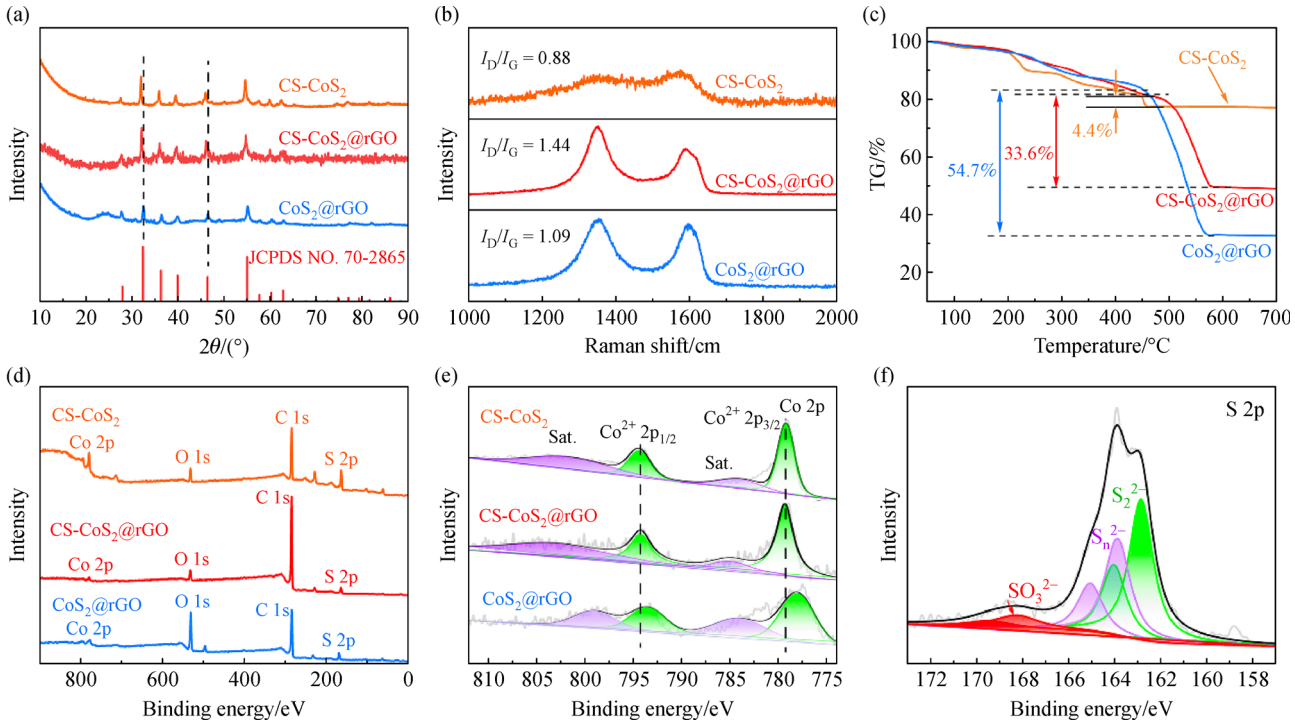

Fig. 2 (a) XRD patterns, (b) Raman spectra, (c) TG curves, (d) XPS survey spectra and (e) Co 2p deconvolution XPS spectra of three samples; (f) S 2p deconvolution XPS spectra of CS-CoS_2@rGO.

shown in Fig. 2(c). The weight loss observed before 200 °C is mainly due to the volatilization of adsorbed water, and weight loss of 200 °C to 450 °C stems from the oxidation of metal sulfides in the air [23]. Combustion of various carbon is known to be associated with the weight loss from 450 °C to 600 °C [24]. For CS-CoS_2, the 4.4% mass loss above 450 °C proves that L-cysteine generated *in situ* doped pyrolytic carbon during the hydrothermal process. In other words, it illustrates that there exists *in situ* doped carbon in CS-CoS_2 and CS-CoS_2@rGO.

The XPS spectra used to characterize the elemental composition and state are shown in Figs. 2(d), 2(e), and 2(f). The survey spectra of these three samples all demonstrate the peaks of C 1s, Co 2p, and S 2p, which proves the successful preparation of the CoS_2@rGO composite material (Fig. 2(d)). As can be seen from the Co 2p deconvolution results in Fig. 2(e) that only one state of Co^{2+} exists in three samples due to the typical Co^{2+} $2p_{3/2}$ and Co^{2+} $2p_{1/2}$ peaks with the binding energy difference of 15 eV for spin-orbit splitting and the two characteristic satellite peaks [25]. Compared with CoS_2@rGO, the Co^{2+} $2p_{3/2}$ and Co^{2+} $2p_{1/2}$ peaks of CS-CoS_2 and CS-CoS_2@rGO are slightly shifted to the higher binding energy position. Such a shift is due to the interstitial doped carbon affecting the electronic structure of Co^{2+}, indicating that the sulfur source of L-cysteine introduced doped carbon into CS-CoS_2 and CS-CoS_2@rGO [12]. The S 2p high-resolution XPS spectrum of CS-CoS_2@rGO is shown in Fig. 2(f), where the peak near 168.5 eV is attributed to SO_3^{2-} derived from the oxidation of surface sulfur in the air [26]. The peak near 162.9 eV corresponds to the existence of S_2^{2-}, indicating the successful Synthesis of CoS_2 [19]. Besides, the peak at about 163.9 eV is attributed to the polymer S_n^{2-}, which is beneficial to the anchoring of CoS_2 to rGO sheets and implies the presence of unsaturated sulfur [13,25]. After the sensitivity factor calibration, the calculated atomic ratio of S and Co in CS-CoS_2 and CS-CoS_2@rGO is roughly 6:1, which is far beyond that of in CoS_2@rGO (2.2:1) and the stoichiometric ratio of CoS_2 (Table S2, cf. ESM). However, EDS test results show that the atomic ratio of Co and S (about 2.3:1) in CS-CoS_2 and CS-CoS_2@rGO only slightly above the stoichiometric ratio (Table S1). The above element ratios illustrate that there exists abundant unsaturated sulfur on the surface of CS-CoS_2 and CS-CoS_2@rGO, which can be active sites for lithium storage and increase the contribution ratio of pseudocapacitive energy storage [17]. Furthermore, the test results of EDS and XPS both show that there is no unsaturated sulfur deviates from the stoichiometric ratio in CoS_2@rGO (Tables S1 and S2).

3.2 Electrochemical performance of anode materials

First, half-cells were assembled to study the lithium storage performance of the LIC anode. By changing the concentration of other reagents without changing the amount of graphene, the best CoS_2 loading mass on

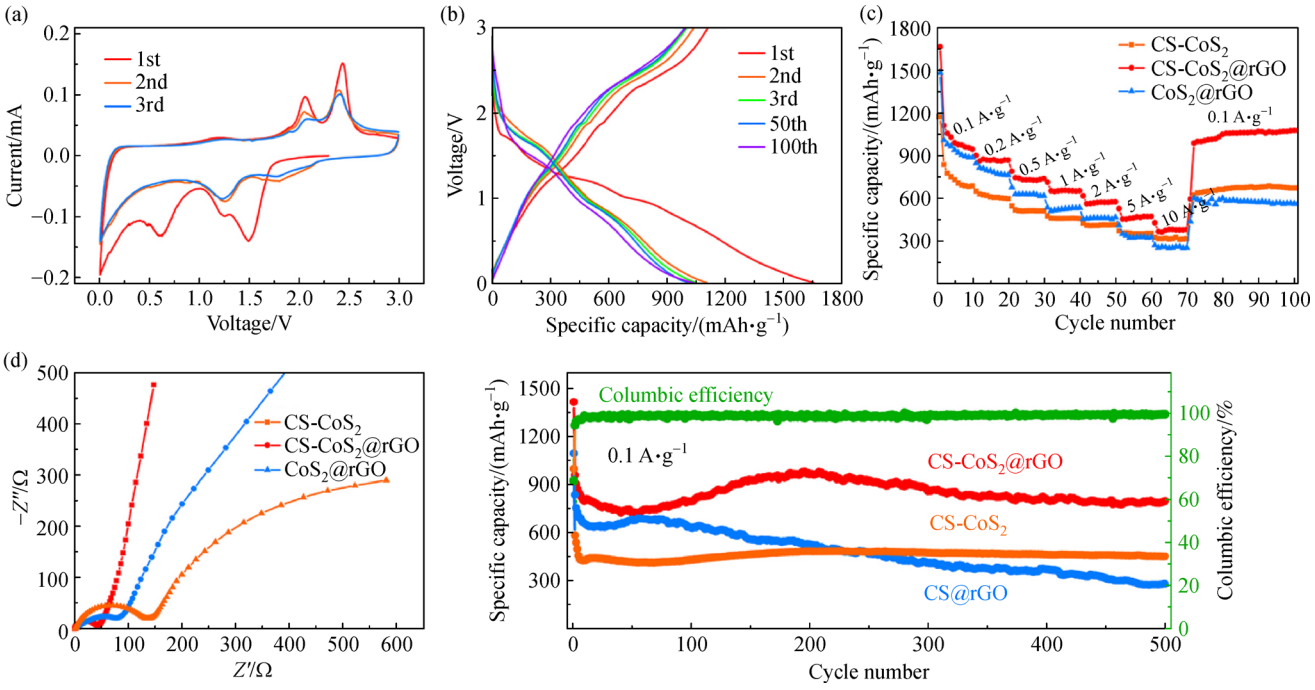

Fig. 3 (a) CV curves at 0.1 $mV \cdot s^{-1}$ from 0.01 to 3 V and (b) charge/discharge curves at 0.1 $A \cdot g^{-1}$ of CS-CoS_2@rGO; (c) rate performance, (d) EIS spectra, and (e) cycle performance at 1 $A \cdot g^{-1}$ of three samples.

graphene is obtained (Fig. S4, cf. ESM). Figure 3 shows the electrochemical performance of the three samples. Figure 3(a) shows the CV curves of CS-CoS_2@rGO, which is measured in the voltage range of 0.01 to 3 V at the scan rate of 0.1 $mV \cdot s^{-1}$. In the initial cycle, the cathodic peaks locating at about 1.5 and 1.3 V result from the formation of Li_xCoS_2 and subsequent reduction to Li_2S and Co and then move to around 1.8 and 1.2 V [27]. The cathodic peak of approximately 0.6 V that only appears in the initial cycle, is associated with the formation of the solid-electrolyte interphase (SEI) layer [23]. During the subsequent de-lithiation process, the oxidation of Co to CoS_2 causes the anodic peak signals at about 2.4 and 2.1 V [19]. Since then, the peaks at different positions overlap, indicating that the material has excellent cyclic reversibility. According to the sufficient verification of previous studies, the reaction mechanism during charge and discharge can be expressed by Eqs. (1) and (2):

$$CoS_2 + xLi^+ + xe^- \rightleftharpoons LixCoS_2 \quad (1)$$

$$LixCoS_2 + (4-x)Li^+ + (4-x)e^- \rightleftharpoons 2Li_2S + Co \quad (2)$$

The unique carbon doping and the rich unsaturated sulfur on the surface of CS-CoS_2@rGO promote initial charge/discharge specific capacity to 1660.2 and 1110.8 $mAh \cdot g^{-1}$ (Fig. 3(b)). The inevitable and irreversible capacity loss is caused by the formation of the SEI film, making the initial coulombic efficiency of 66.8% [28]. After that, the coulombic efficiency increased to 99% after only a few cycles, indicating that the superior cycle stability of CS-CoS_2@rGO after the formation of SEI film. Surprisingly, the material still shows a high specific capacity of 1048.7 $mAh \cdot g^{-1}$ after 100 cycles at 0.1 $A \cdot g^{-1}$ (Fig. 3(b)). The above data exceeding the theoretical capacity of CoS_2 (870 $mAh \cdot g^{-1}$) may be inferred to come from polymer/gel-like film, space charge, and interfacial storage of the metallic nanograins formed when discharge to low potentials, considering the similarity between TMSs and corresponding oxides [29]. In Fig. 3(c), CS-CoS_2@rGO with the improved reaction kinetic shows much superior rate performance than CoS_2@rGO and CS-CoS_2, and can retain a high specific capacity of 380.8 $mAh \cdot g^{-1}$ even at 10 $A \cdot g^{-1}$. Besides, when the current returned to 0.1 $A \cdot g^{-1}$ after cycling at different current densities, the specific capacity of CS-CoS_2@rGO returns to 1077.6 $mAh \cdot g^{-1}$, which is even higher than the original specific capacity at 0.1 $A \cdot g^{-1}$ due to the electro-activation [30]. This demonstrates that the excellent structural stability and cycle reversibility of the CS-CoS_2@rGO, which can withstand different current densities. As described in Fig. 3(d), compared with CS-CoS_2 and CoS_2@rGO, CS-CoS_2@rGO has the faster reaction kinetic for its smaller semicircle shown in the high-frequency region and more rapid lithium-ion diffusion due to its greater slope in the low-frequency region [31]. Furthermore, CS-CoS_2@rGO also shows much better cycle performance than CS-CoS_2 and CoS_2@rGO. It can still maintain a high specific capacity of 810 $mAh \cdot g^{-1}$ after being cycled at 1 $A \cdot g^{-1}$ for 500 cycles, and the observed apparent increase of capacity during the cycle can be due to

the electro-activation process [30]. To conclude, the unique carbon doping and enriched surface unsaturated sulfur of CS-CoS_2@rGO has enhanced its reaction kinetic and ion diffusion, making it possessed super-excellent electrochemical performance in all aspects.

Galvanostatic intermittent titration technique (GITT) measurements and CV tests with scan rates ranging from 0.1 to 1 mV·s^{-1} were performed (Fig. 4) to investigate the electrochemical kinetic and energy storage type of CS-CoS_2@rGO and CoS_2@rGO. The specific operation of GITT tests and the simplified process of calculation formula can be found in the supporting information. In short, since there is a basic regular linear relationship between the voltage (V) and the square root of the relaxation time ($\tau_{0.5}$) in Figs. 4(c) and 4(d), the lithium-ion diffusion coefficient (D_{Li+}) can be calculated by Eq. (3) [32]:

$$D_{Li+} = \frac{4}{\pi\tau}\left(\frac{m_B V_M}{M_B A}\right)^2 \left(\frac{\Delta E_S}{\Delta E_\tau}\right)^2, \quad (3)$$

where m_B, V_M, M_B, and A represent the loading mass, molar volume, molar mass, and contact area with electrolyte of active materials, respectively. Moreover, the voltage change (ΔE_τ) caused by pulse and voltage change (ΔE_s) caused by discharge is described in Figs. 4(a) and 4(b). As shown in Fig. 4(e), the lithium-ion diffusion coefficients of CS-CoS_2@rGO and CoS_2@rGO show the same trend at different potentials, indicating that the lithium storage mechanism of them are the same [32]. Notably, the lithium-ion diffusion coefficient of CS-CoS_2@rGO is higher than that of CoS_2@rGO at all potentials. The faster ion diffusion of CS-CoS_2@rGO will be beneficial to improve electrochemical kinetic without a doubt. The rapid lithium-ion diffusion of CS-CoS_2@rGO

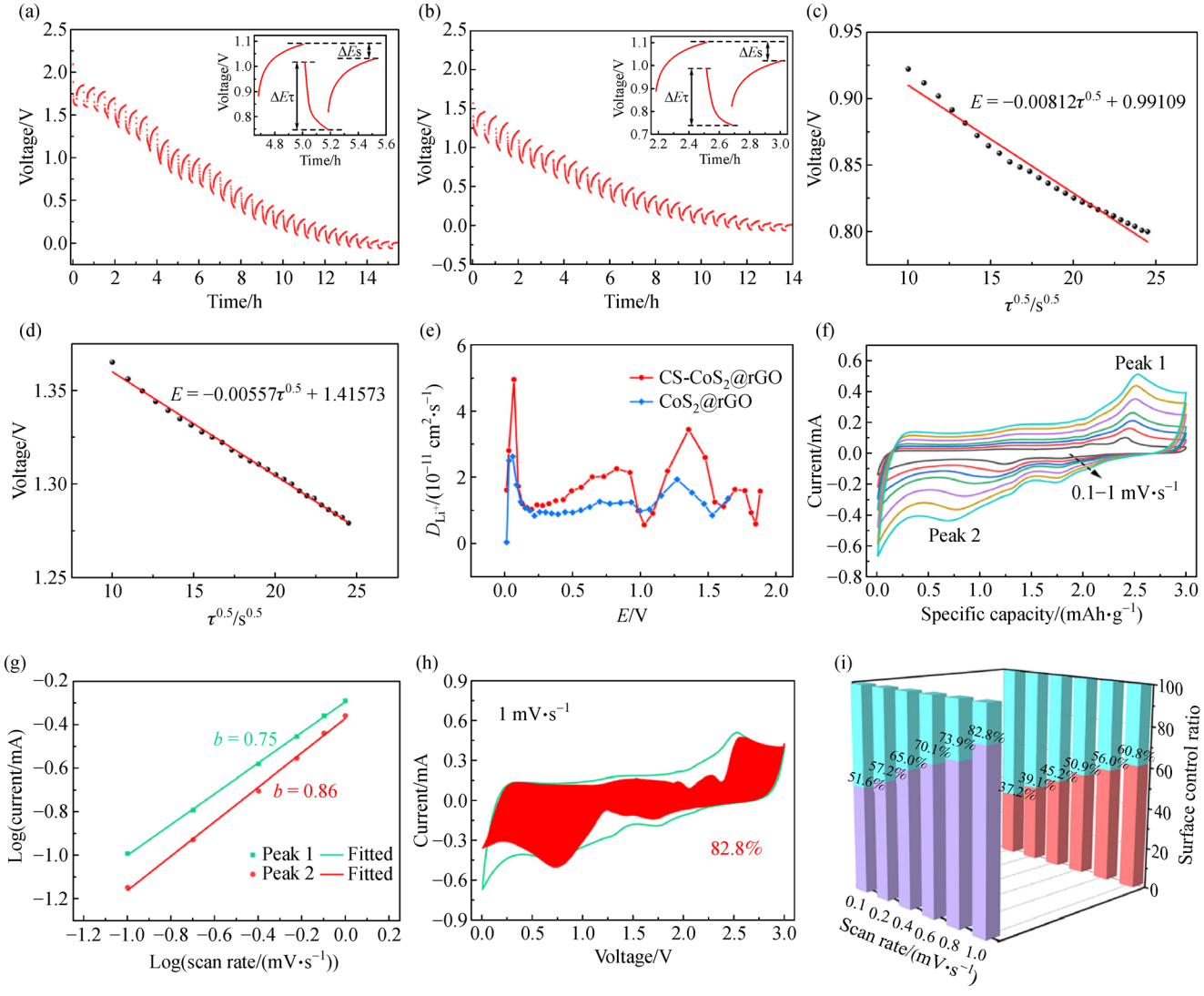

Fig. 4 GITT curves of (a) CS-CoS_2@rGO and (b) CoS_2@rGO; (c and d) linear fit of V and $\tau^{0.5}$; (e) Li^+ diffusion coefficients of CS-CoS_2@rGO and CoS_2@rGO; (f) CV curves of CS-CoS_2@rGO at different scan rates; (g) b values of CS-CoS_2@rGO; (h) capacitance contribution at 1 mV·s^{-1}; (i) capacitance contribution at different scan rates.

is the result of the combined effect of carbon doping and large surface unsaturated sulfur. It corresponds to the EIS results and the excellent rate/cycle performance.

Figure 4(f) contains CV curves of CS-CoS_2@rGO at different scan rates, where the scan rate (v) and peak current (i) conform to Eq. (4) [10]:

$$i = av^b. \tag{4}$$

In the above formula, a and b are variable constants, with b varying between 0.5 and 1. The higher value of b means that the electrochemical process is mainly controlled by pseudocapacitance; otherwise, it is mainly controlled by diffusion. The b values of peak 1 and peak 2 in Fig. 4(f) is calculated to be 0.75 and 0.86, respectively. The value of b shows that for CS-CoS_2@rGO, the pseudocapacitive energy storage contributes a large percentage of the whole energy storage. Furthermore, the specific proportion of pseudocapacitance-controlled energy storage and diffusion-controlled energy storage can be obtained by Eq. (5) [10]:

$$i = k_1 v + k_2 v^{1/2}, \tag{5}$$

where i represents the current under the corresponding voltage (V), and $k_1 v$ and $k_2 v^{1/2}$ represent the current of pseudocapacitive control and diffusion control, respectively. After calculation and fitting, the fitting graph of pseudocapacitive contribution at 1 $mV \cdot s^{-1}$ is shown in Fig. 4(h). The percentage of pseudocapacitive contribution at different scan rates is shown in Fig. 4(i), which is much higher than CoS_2@rGO to reveal that the electrochemical process of CS-CoS_2@rGO material is dominated by pseudocapacitive control. In contrast, the b value and the pseudocapacitive contribution percentage of CoS_2@rGO are significantly lower than that of CS-CoS_2@rGO, indicating that the methods of promoting the pseudocapacitive contribution of CS-CoS_2@rGO are effective.

3.3 Characterization of cathode materials

The electrochemical performance of biochar depends on not only the effect of the carbonization and activation conditions but also the characteristics of the raw material itself [33]. To give full play to the potential of crabapple leaves for activated carbon, two types of raw materials, dead leaves and green leaves, were directly pyrolyzed to produce activated carbon. Thus, to compare and select the best raw material (C-D and C-G), and the best preparation process was chosen by direct pyrolysis and hydrothermal pyrolysis of dead leaves (C-H). Figure 5 compares the differences in composition and structure between the three carbons. Generally, plant tissues are mainly composed of cellulose, hemicellulose, and lignin [33]. As for crabapple leaves, cellulose with a hydrothermal carbonization temperature between 160 °C and 170 °C is the main constituent [34]. To ensure the full hydrothermal carbonization of raw material, 180 °C is selected as the hydrothermal temperature. A certain amount of concentrated sulfuric acid is used to promote the dehydration polymerization reaction to catalyze the carbonization [35].

In Figs. 5(a) and 5(b), both C-D and C-G present irregular lumps, and the porous structure cannot be directly observed on their smooth surfaces. However, the rough surface of the fracture cross-section may indicate the existence of pores among the block. In Fig. 5(c), C-H exhibits a honeycomb-like structure composed of sheets with uneven thickness, which can provide a shorter ion diffusion path than the bulk frame and may be beneficial to electric double layer capacitance [36]. The structural particularity of C-H is derived from the difference in mechanism between direct pyrolysis at high temperature and hydrothermal carbonization, which involves a series of reaction processes of dehydration, condensation, polymerization, and aromatization [33]. In Fig. 5(d), the nitrogen adsorption/desorption curves of C-D, C-G, and C-H all demonstrate typical characteristics of I/IV type isotherms, indicating that abundant micropores and mesopores exist on these three samples [37]. The calculated related parameters of pore structure are shown in Fig. 5(e), where C-G has the highest surface area of 2621.89 $m^2 \cdot g^{-1}$, and C-D has the smallest average pore size and a higher mesopore distribution than C-G. The smallest specific surface area and the largest average pore diameter of C-H indicate that a large number of micropores collapsed to larger pores during the activation process, which corresponds to the fragmentation morphology in Fig. 5(c). The (002), (100) X-ray diffraction peaks in Fig. 5(f) and the D-band, G-band of the Raman spectrum in Fig. 5(g) are typical characteristics of carbon materials [38]. In addition, the intensity ratios of D-band and G-band of the three samples in Fig. 5(g) are basically around 1 with no significant difference, indicating that the disorder of them are the same [39]. In Fig. 5(h), the XPS survey spectra of C-D, C-G, and C-H all show the presence of C, O, and S elements. Here, the sulfur doping amounts of C-D, C-G, and C-H are 1.85 at%, 1.70 at%, and 3.47 at%, respectively, with no significant disparity (Table S3, cf. ESM). The size and electronegativity of doped sulfur atoms are different from carbon, which can change the electronic structure of surrounding carbon atoms, thereby reducing charge transfer resistance and improving electrode wettability [40].

3.4 Electrochemical performance of cathode materials

The potential extended range of 1.5–4.3 V is used to maximize the specific capacity, ensure electrolyte stability and narrow the capacity gap between the cathode and anode [6]. The electrochemical performance of cathode materials is shown in Fig. 6. The CV curves of C-D appear as the quasi-rectangular shape with certain distortion. Comparing with C-G and C-H, C-D has a larger enclosed

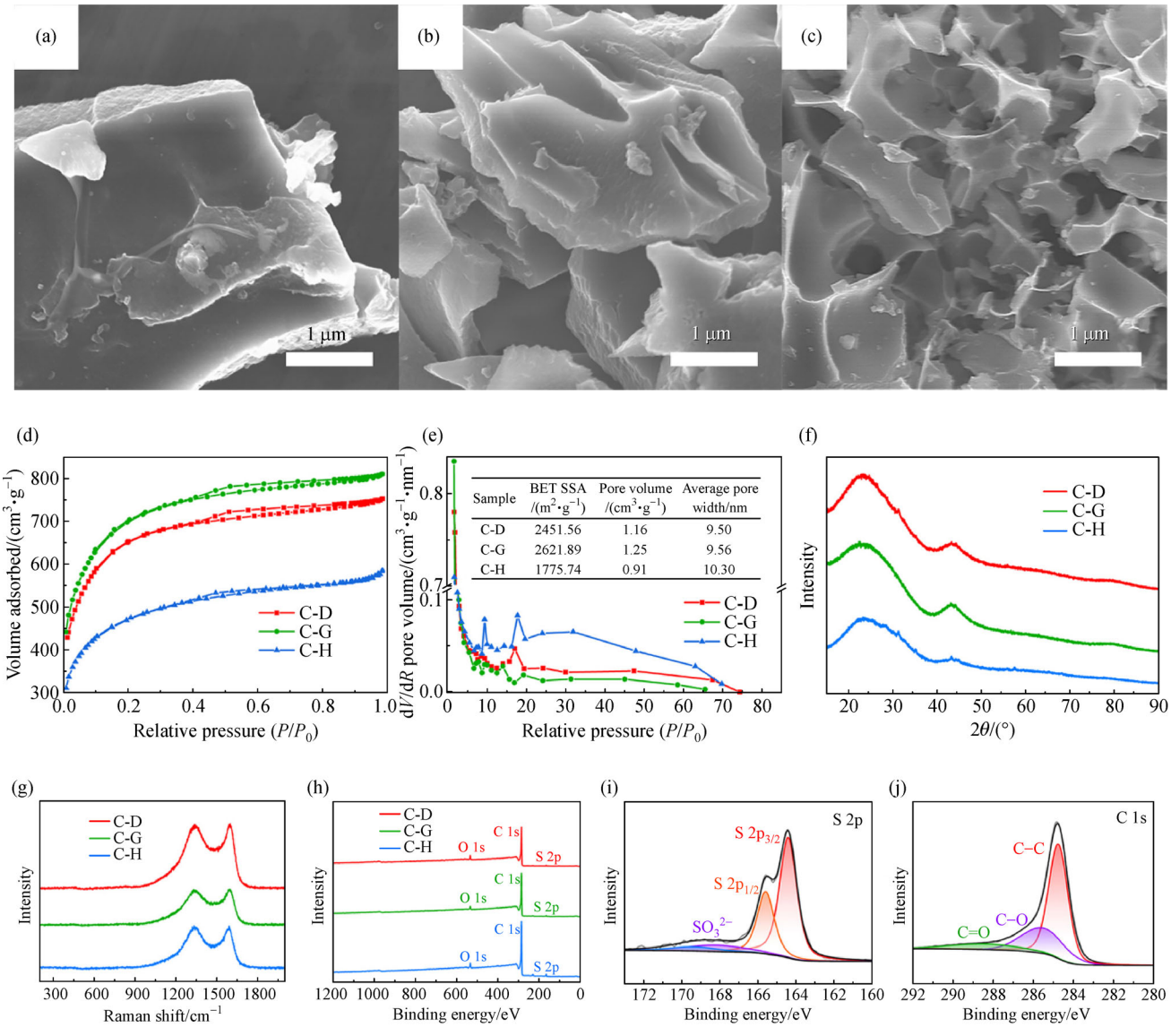

Fig. 5 SEM images of (a) C-D, (b) C-G, and (c) C-H; (d) nitrogen desorption/adsorption curves, (e) pore size distribution, (f) XRD patterns, (g) Raman spectra, and (h) XPS survey spectra of C-D, C-G and C-H; (i) S 2p and (j) C 1s deconvolution XPS spectra of C-D.

area as well as the largest specific capacity (Figs. 6(a) and 6(b)) [41]. The GCD curves of the three samples are all symmetric linear shapes, and the IR drops are very small, indicating good capacitance characteristics and small electrode internal resistance (Figs. 6(c) and 6(d)) [40]. After calculation, the specific capacities of C-D, C-G, and C-H at 0.1 $A \cdot g^{-1}$ are 114.2, 107.2, and 95.5 $mAh \cdot g^{-1}$, respectively. Generally, activated carbon materials storage energy mainly relies on electric double-layer capacitance, which is directly related to the specific surface area [37]. This means that the greater the specific surface area of the porous carbon, the greater the specific capacitance. However, the specific capacitance of the three samples here does not conform to this law. The reason why C-D has a smaller specific surface area than C-G, but higher specific capacity should be that the more appropriate hierarchical pore structure of C-D, which means more mesopores. Some previous studies have proved that electrolyte ions are difficult to enter the most existing micropores. So, in this case, more mesopores can be used as rapid ion diffusion channels for improving the utilization rate of specific surface areas to obtain higher electrochemical performance [36,38]. Similarly, abundant mesopores also enhance the performance of C-H. The composition of dead leaves and green leaves is the main factor for the difference of C-D and C-G porous structure. In the process of leaf dying, as the organic matter is consumed, the proportion of inorganic salts in the leaves increase accordingly [42]. These inorganic mineral elements have the same ability as KOH to form pores and activate carbon materials [43]. In this way, the micropores are further enlarged and ultimately improve the distribution of mesopores. After

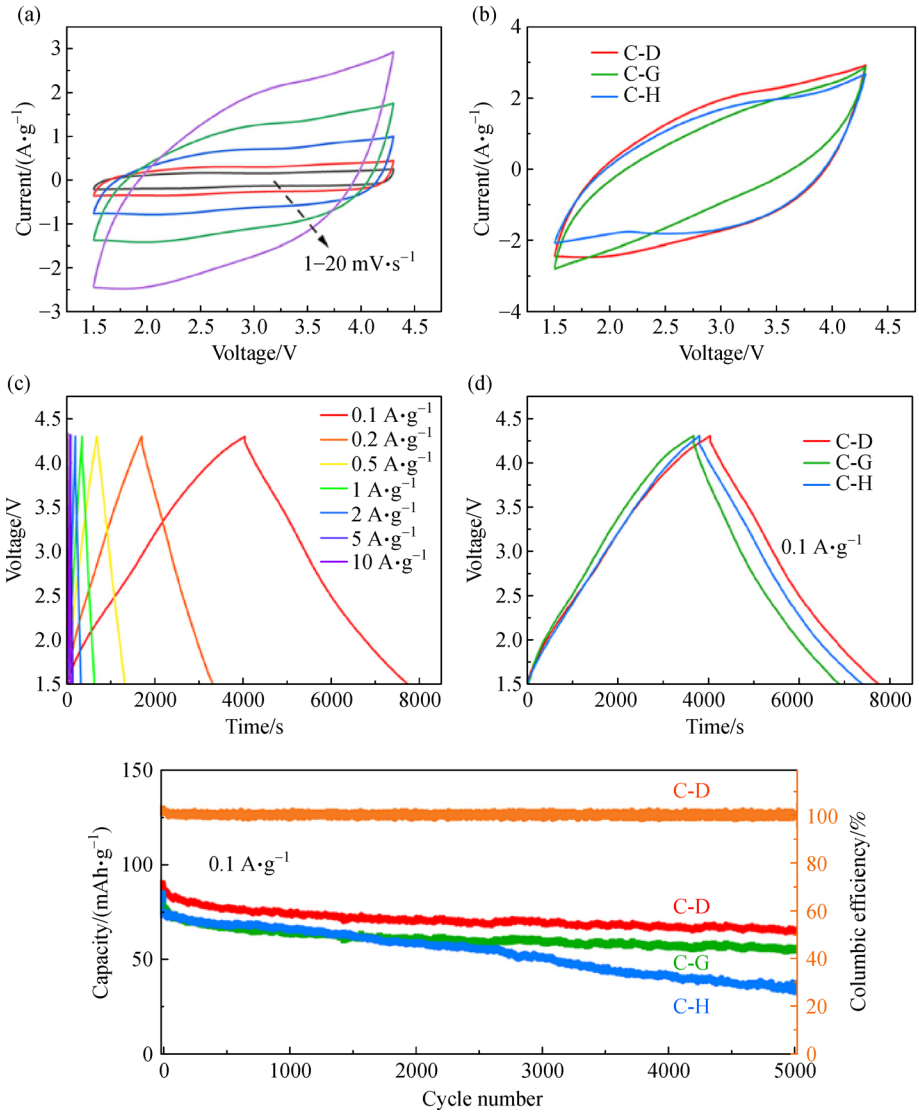

Fig. 6 (a) CV curves of C-D at different scan rates; (b) CV curves of C-D, C-G, and C-H at 0.1 mV·s^{-1}; (c) GCD curves of C-D at different current densities; (d) GCD curves at 0.1 A·g^{-1} and (e) cycle performance at 1 A·g^{-1} of C-D, C-G, and C-H.

being cycled for 5000 weeks at a high current density of 1 A·g^{-1}, the specific capacity retention rate of C-D is still as high as 66.3%, confirming the excellent cycle stability of C-D. Despite the above analysis and verification, C-H and C-D have a suitable pore structure, but the performance of C-H is not stable, which can be seen from the cycle stability in Fig. 5(e). In short, the C-D derived from dead leaves and prepared through direct pyrolysis and activation at high temperature demonstrates the most superior electrochemical performance among the three samples.

3.5 Electrochemical performance of LIC

To alleviate the electrolyte consumption problem of LICs, the CS-CoS_2@rGO anode is pre-lithiated before assembling. The most troublesome flaw hindering the practical application of LICs is the difficulty of matching the anode and cathode reaction kinetic and capacity. The energy storage method and final electrochemical performance of LICs can be shown in Fig. 7. The energy storage mechanism of LICs can be simply described as the lithium ions adsorption on the cathode and insertion into anode during the charging process (Fig. 7(a)) [4]. However, two energy storage mechanisms, Li^+ ion desorption and PF_6^- ion adsorption, actually occur within such a potential extended range of the cathode [44]. Therefore, the potential interval of the LICs is adjusted to 1 to 4.3 V (Fig. 7(b)) [6]. To ensure the safety and electrochemical performance of LIC, the charge on two electrodes should be balanced. Conforming to the charge balance principle ($Q_{cathode} = Q_{anode}$), the calculated mass ratio of the cathode and anode should be 3:1 [45]. After further verifying the electrochemical performance under different mass ratios, it

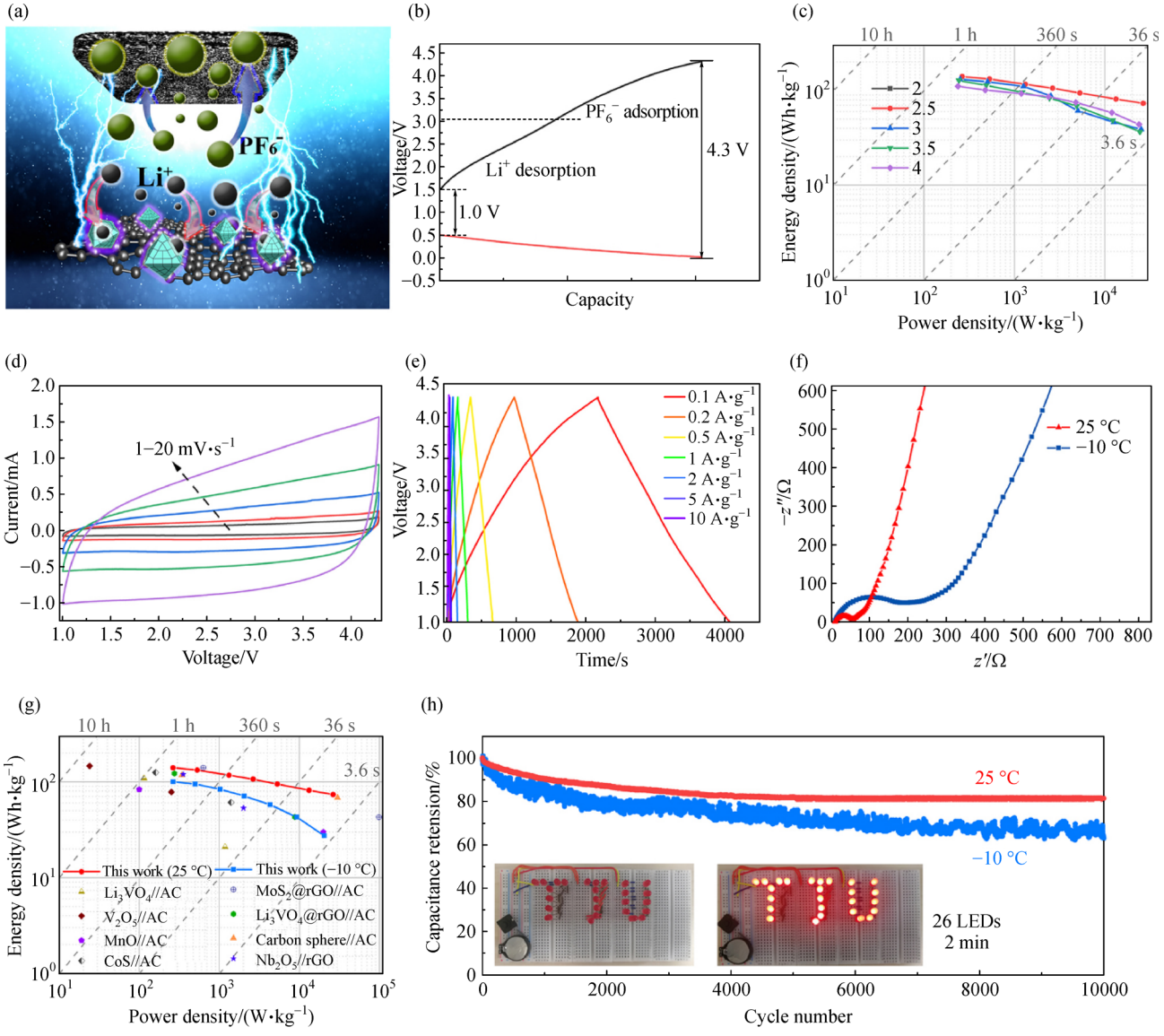

Fig. 7 Electrochemical performance of the assembled LIC: (a) schematic diagram of energy storage mechanism, (b) GCD curves of anode and cathode, (c) Ragone diagram under different mass ratios of cathode and anode, (d) CV curves from 1 to 20 mV·s^{-1}, (e) GCD curves at different current densities, (f) EIS spectra at 25 °C and –10 °C, (g) Ragone plots of this work and the recent reports, and (h) cycle performance at 25 °C and –10 °C.

is finally determined that the mass ratio of the cathode and anode is 2.5:1 (Fig. 7(c)). In Fig. 7(d), the LIC exhibits the shape that approximates an ideal rectangle at different scanning rates or even a high scanning rate of 20 mV·s^{-1}, revealing the excellent reaction kinetic matching between cathode and anode [46]. The GCD curves in Fig. 7(e) also illustrate the superior capacitive performance of LIC due to the regular linearity symmetry characteristics and shallow IR voltage drop [47]. The EIS spectrum of the entire assembled LICs device is shown in Fig. 7(f). The inherent internal resistance and charge transfer resistance of the assembled LICs are meager, and the significant slope of the diagonal line indicates rapid ion diffusion. To demonstrate and compare energy density/power density, the drawn Ragone diagram is shown in Fig. 7(g), where it can be seen that the performance of the assembled LICs is at the leading level of the previous reports [4,6]. The formulas for calculating energy density/power density based on constant current charge and discharge are as follows [8], where the discharge current density i_m is calculated by Eqs. (6) and (7):

$$E = i_m \int_{t_1}^{t_2} V \mathrm{d}t, \tag{6}$$

$$P = E/\Delta t, \tag{7}$$

where V represents the potential (V) and t represents time (h) during the discharge process. The assembled LIC exhibits a high energy density of 132.9 $Wh \cdot kg^{-1}$ at a power density of 265 $W \cdot kg^{-1}$, and 50.0 $Wh \cdot kg^{-1}$ even at 26.5 $kW \cdot kg^{-1}$. In Fig. 7(h), the exceptional capacitance retention rate of 81.5% even after 10000 cycles at 1 $A \cdot g^{-1}$ reveals the outstanding cycle performance of the LIC. Furthermore, to verify the practical application potential, the low-temperature electrochemical performance of LIC was also tested (Figs. 7(f), 7(g), and 7(h)). It can be seen that the electrochemical properties of the assembled LICs remain at satisfactory levels even at –10 °C. Surprisingly, the energy and power density are still comparable with previous reports (Fig. 7(g)), and LIC still retains fast ion diffusion (Fig. 7(f)). Although the cycle stability at –10 °C fluctuates, there is still an energy density retention rate of 63.4%. The above results reveal that the capacity and kinetic of the assembled LIC electrodes are well matched, which determines the stable superior electrochemical performance and ultra-high-energy/power density of the LIC.

4 Conclusions

All in all, we have prepared CoS_2@rGO composite anode and biomass activated carbon cathode. For the anode, based on the graphene conductive network, *in situ* carbon doping and surface unsaturated sulfur are further introduced, which have been verified to improve the reaction kinetic of the anode fully. For the cathode, the C-D with the best performance is selected from different raw materials and other preparation methods. Through the reasonable design of two electrodes as well as careful balancing and matching of two electrodes, the final assembled LIC exhibits excellent electrochemical performance at room temperature and low temperature. The work will provide some reference for the novel using TMS as the anode material of LIC and some strategies further to develop the LIC with high energy and power density.

Acknowledgements This work is supported by the National Natural Science Foundation of China (Grant Nos. 51772205 and 51772208), and the General Program of Municipal Natural Science Foundation of Tianjin (Grant Nos. 17JCYBJC17000 and 17JCYBJC22700).

Electronic Supplementary Material Supplementary material is available in the online version of this article at https://doi.org/10.1007/s11705-021-2086-2 and is accessible for authorized users.

References

1. Aravindan V, Gnanaraj J, Lee Y S, Madhavi S. Insertion-type electrodes for nonaqueous Li-ion capacitors. Chemical Reviews, 2014, 114(23): 11619–11635
2. Jiang X P, Li Z Y, Lu G J, Hu N, Ji G P, Liu W, Guo X L, Wu D, Liu X J, Xu C H. Pores enriched $CoNiO_2$ nanosheets on graphene hollow fibers for high performance supercapacitor-battery hybrid energy storage. Electrochimica Acta, 2020, 358: 136857
3. Wang R H, Zhao Q N, Zheng W K, Ren Z L, Hu X L, Li J, Lu L, Hu N, Molenda J, Liu X J, et al. Achieving high energy density in a 4.5 V all nitrogen-doped graphene based lithium-ion capacitor. Journal of Materials Chemistry. A, Materials for Energy and Sustainability, 2019, 7(34): 19909–19921
4. Wang Y K, Liu M C, Cao J Y, Zhang H J, Kong L B, Trudgeon D P, Li X H, Walsh F C. 3D hierarchically structured CoS nanosheets: Li^+ storage mechanism and application of the high-performance lithium-ion capacitors. ACS Applied Materials & Interfaces, 2020, 12(3): 3709–3718
5. Xing T, Ouyang Y H, Zheng L P, Wang X Y, Liu H, Chen M F, Yu R Z, Wang X Y, Wu C. Free-standing ternary metallic sulphides/Ni/C-nanofiber anodes for high-performance lithium-ion capacitors. Journal of Energy Chemistry, 2020, 42: 108–115
6. Zhan C Z, Liu W, Hu M X, Liang Q H, Yu X L, Shen Y, Lv R T, Kang F Y, Huang Z H. High-performance sodium-ion hybrid capacitors based on an interlayer-expanded MoS_2/rGO composite: surpassing the performance of lithium-ion capacitors in a uniform system. NPG Asia Materials, 2018, 10(8): 775–787
7. Wang Q F, Zou R Q, Xia W, Ma J, Qiu B, Mahmood A, Zhao R, Yang Y C, Xia D G, Xu Q. Facile synthesis of ultrasmall CoS_2 nanoparticles within thin N-doped porous carbon shell for high performance lithium-ion batteries. Small, 2015, 11(21): 2511–2517
8. Wang H W, Guan C, Wang X F, Fan H J. A high energy and power Li-ion capacitor based on a TiO_2 nanobelt array anode and a graphene hydrogel cathode. Small, 2015, 11(12): 1470–1477
9. Yuan X Q, Liu B C, Hou H J, Zeinu K, He Y H, Yang X R, Xue W J, He X L, Huang L, Zhu X L, et al. Facile synthesis of mesoporous graphene platelets with *in situ* nitrogen and sulfur doping for lithium-sulfur batteries. RSC Advances, 2017, 7(36): 22567–22577
10. Augustyn V, Simon P, Dunn B. Pseudocapacitive oxide materials for high-rate electrochemical energy storage. Energy & Environmental Science, 2014, 7(5): 1597–1614
11. Wu Z C, Li B E, Xue Y J, Li J J, Zhang Y L, Gao F. Fabrication of defect-rich MoS_2 ultrathin nanosheets for application in lithium-ion batteries and supercapacitors. Journal of Materials Chemistry. A, Materials for Energy and Sustainability, 2015, 3(38): 19445–19454
12. Zhao D Q, Zong W J, Fan Z H, Xiong S M, Du M, Wu T H, Fang Y W, Ji F Y, Xu X. Synthesis of carbon-doped $BiVO_4$@multi-walled carbon nanotubes with high visible-light absorption behavior, and evaluation of their photocatalytic properties. CrystEngComm, 2016, 18(47): 9007–9015
13. Natarajan S, Lee Y S, Aravindan V. Biomass-derived carbon materials as prospective electrodes for high-energy lithium- and sodium-ion capacitors. Chemistry, an Asian Journal, 2019, 14(7): 936–951
14. Zhang B, Ye X C, Hou W Y, Zhao Y, Xie Y. Biomolecule-assisted synthesis and electrochemical hydrogen storage of Bi_2S_3 flowerlike patterns with well-aligned nanorods. Journal of Physical Chemistry B, 2006, 110(18): 8978–8985
15. Xie X Q, Ao Z M, Su D W, Zhang J Q, Wang G X. MoS_2/graphene composite anodes with enhanced performance for sodium-ion batteries: the role of the two-dimensional heterointerface. Advanced

Functional Materials, 2015, 25(9): 1393–1403
16. Wang X, Li X Y, Li Q, Li H S, Xu J, Wang H, Zhao G X, Lu L S, Lin X Y, Li H L, et al. Improved electrochemical performance based on nanostructured SnS_2@CoS_2-rGO composite anode for sodium-ion batteries. Nano-Micro Letters, 2018, 10(3): 46
17. Li W D, Wang D Z, Song Z H, Gong Z J, Guo X S, Liu J, Zhang Z H, Li G C. Carbon confinement synthesis of interlayer-expanded and sulfur-enriched MoS_{2+x} nanocoating on hollow carbon spheres for advanced Li-S batteries. Nano Research, 2019, 12(11): 2908–2917
18. Xu Y X, Sheng K X, Li C, Shi G Q. Self-assembled graphene hydrogel via a one-step hydrothermal process. ACS Nano, 2010, 4 (7): 4324–4330
19. Singh V, Tiwari A, Nagaiah T C. Facet-controlled morphology of cobalt disulfide towards enhanced oxygen reduction reaction. Journal of Materials Chemistry. A, Materials for Energy and Sustainability, 2018, 6(45): 22545–22554
20. Yu J X, Chen Z G, Zeng L, Ma Y Y, Feng Z, Wu Y, Lin H J, Zhao L H, He Y M. Synthesis of carbon-doped $KNbO_3$ photocatalyst with excellent performance for photocatalytic hydrogen production. Solar Energy Materials and Solar Cells, 2018, 179: 45–56
21. Tang J H, Shen J F, Li N, Ye M X. A free template strategy for the synthesis of CoS_2-reduced graphene oxide nanocomposite with enhanced electrode performance for supercapacitors. Ceramics International, 2014, 40(A): 15411–15419
22. Meng Z D, Zhu L, Ullah K, Ye S, Oh W C. Detection of oxygen species generated by CNT photosensitized CoS_2 nanocomposites. Applied Surface Science, 2013, 286: 261–268
23. Ye J B, Ma L, Chen W X, Ma Y J, Huang F H, Gao C, Lee J Y. Supramolecule-mediated synthesis of MoS_2/reduced graphene oxide composites with enhanced electrochemical performance for reversible lithium storage. Journal of Materials Chemistry. A, Materials for Energy and Sustainability, 2015, 3(13): 6884–6893
24. Ma L, Huang G C, Chen W X, Wang Z, Ye J B, Li H Y, Chen D Y, Lee J Y. Cationic surfactant-assisted hydrothermal synthesis of few-layer molybdenum disulfide/graphene composites: microstructure and electrochemical lithium storage. Journal of Power Sources, 2014, 264: 262–271
25. Zhu L, Susac D, Teo M, Wong K C, Wong P C, Parsons R R, Bizzotto D, Mitchell K A R, Campbell S A. Investigation of CoS_2-based thin films as model catalysts for the oxygen reduction reaction. Journal of Catalysis, 2008, 258(1): 235–242
26. Yang Y, Zhang K, Lin H, Li X, Chan H C, Yang L, Gao Q. MoS_2-Ni_3S_2 heteronanorods as efficient and stable bifunctional electrocatalysts for overall water splitting. ACS Catalysis, 2017, 7(4): 2357–2366
27. Jiao Z, Zhao P D, He Y C, Ling L, Sun W F, Cheng L L. Mesoporous yolk-shell CoS_2/nitrogen-doped carbon dodecahedron nanocomposites as efficient anode materials for lithium-ion batteries. Journal of Alloys and Compounds, 2019, 809: 151854
28. Yuan J, Zhu J W, Wang R H, Deng Y X, Zhang S, Yao C, Li Y J, Li X L, Xu C H. 3D few-layered MoS_2/graphene hybrid aerogels on carbon fiber papers: a free-standing electrode for high-performance lithium/sodium-ion batteries. Chemical Engineering Journal, 2020, 398: 125592
29. He J R, Chen Y F, Li P J, Fu F, Wang Z G, Zhang W L. Self-assembled CoS_2 nanoparticles wrapped by CoS_2-quantum-dots-anchored graphene nanosheets as superior-capability anode for lithium-ion batteries. Electrochimica Acta, 2015, 182: 424–429
30. Zhang Y H, Wang N N, Sun C H, Lu Z X, Xue P, Tang B, Bai Z C, Dou S X. 3D spongy CoS_2 nanoparticles/carbon composite as high-performance anode material for lithium/sodium ion batteries. Chemical Engineering Journal, 2018, 332: 370–376
31. Wang H C, Cui Z, Fan C Y, Liu S Y, Shi Y H, Wu X L, Zhang J P. 3D porous CoS_2 hexadecahedron derived from MOC toward ultrafast and long-lifespan lithium storage. Chemistry (Weinheim an der Bergstrasse, Germany), 2018, 24(26): 6798–6803
32. Fan S W, Li G D, Cai F P, Yang G. Synthesis of porous Ni-doped $CoSe_2$/C nanospheres towards high-rate and long-term sodium-ion half/full batteries. Chemistry (Weinheim an der Bergstrasse, Germany), 2020, 26(39): 8579–8587
33. Hu B, Wang K, Wu L H, Yu S H, Antonietti M, Titirici M M. Engineering carbon materials from the hydrothermal carbonization process of biomass. Advanced Materials, 2010, 22(7): 813–828
34. Falco C, Baccile N, Titirici M M. Morphological and structural differences between glucose, cellulose and lignocellulosic biomass derived hydrothermal carbons. Green Chemistry, 2011, 13(11): 3273–3281
35. Hoekman S K, Broch A, Robbins C. Hydrothermal carbonization (HTC) of lignocellulosic biomass. Energy & Fuels, 2011, 25(4): 1802–1810
36. Shu Y, Bai Q H, Fu G X, Xiong Q C, Li C, Ding H F, Shen Y H, Uyama H. Hierarchical porous carbons from polysaccharides carboxymethyl cellulose, bacterial cellulose, and citric acid for supercapacitor. Carbohydrate Polymers, 2020, 227: 115346
37. Shang Y P, Hu X D, Li X, Cai S, Liang G C, Zhao J M, Zheng C M, Sun X H. A facile synthesis of nitrogen-doped hierarchical porous carbon with hollow sphere structure for high-performance supercapacitors. Journal of Materials Science, 2019, 54(19): 12747–12757
38. Zou Z M, Jiang C H. Hierarchical porous carbons derived from leftover rice for high performance supercapacitors. Journal of Alloys and Compounds, 2020, 815: 152280
39. Liu Y, Zhang M Y, Wang L Q, Hou Y J, Guo C X, Xin H Y, Xu S. A biomass carbon material with microtubule bundling and natural *O*-doping derived from goldenberry calyx and its electrochemical performance in supercapacitor. Chinese Chemical Letters, 2020, 31 (3): 805–808
40. Yu X, Park H S. Sulfur-incorporated, porous graphene films for high performance flexible electrochemical capacitors. Carbon, 2014, 77: 59–65
41. Li Y J, Wang G L, Wei T, Fan Z J, Yan P. Nitrogen and sulfur co-doped porous carbon nanosheets derived from willow catkin for supercapacitors. Nano Energy, 2016, 19: 165–175
42. Biswal M, Banerjee A, Deo M, Ogale S. From dead leaves to high energy density supercapacitors. Energy & Environmental Science, 2013, 6(4): 1249–1259
43. Lillo-Rodenas M A, Cazorla-Amoros D, Linares-Solano A. Understanding chemical reactions between carbons and NaOH and KOH: an insight into the chemical activation mechanism. Carbon, 2003, 41 (2): 267–275
44. Aida T, Yamada K, Morita M. An advanced hybrid electrochemical

capacitor that uses a wide potential range at the positive electrode. Electrochemical and Solid-State Letters, 2006, 9(12): 534–536

45. Ding J, Wang H L, Li Z, Cui K, Karpuzov D, Tan X H, Kohandehghan A, Mitlin D. Peanut shell hybrid sodium ion capacitor with extreme energy-power rivals lithium ion capacitors. Energy & Environmental Science, 2015, 8(3): 941–955
46. Luo J M, Zhang W K, Yuan H D, Jin C B, Zhang L Y, Huang H, Liang C, Xia Y, Zhang J, Gan Y P, Tao X. Pillared structure design of MXene with ultralarge interlayer spacing for high-performance lithium-ion capacitors. ACS Nano, 2017, 11(3): 2459–2469
47. Su J T, Wu Y J, Huang C L, Chen Y A, Cheng H Y, Cheng P Y, Hsieh C T, Lu S Y. Nitrogen-doped carbon nanoboxes as high rate capability and long-life anode materials for high-performance Li-ion capacitors. Chemical Engineering Journal, 2020, 396: 125314